J. Shanghai Jiao Tong Univ. (Sci.), 2020
https://doi.org/10.1007/s12204-020-2251-7

Simulation of Bimodal Fiber Distribution Effect on Transient Accumulation of Particles During Filtration

AKAMPUMUZA Obed[1,3], *WU Jiajun*[1] (吴佳骏), *QUAN Zhenzhen*[1,2] (权震震), *QIN Xiaohong*[1*] (覃小红)
(1. College of Textiles, Donghua University, Shanghai 201620, China; 2. Innovation Center for Textile Science and Technology, Donghua University, Shanghai 201620, China; 3. Uganda Industrial Research Institute, P.O. Box 7086, Kampala, Uganda)

Abstract: Modeling has become phenomenal in developing new products. In the case of filters, one of the most applied procedures is via the construction of idealized physical computational models bearing close semblance to real filter media. It is upon these that multi-physics tools were applied to analyze the flow of fluid and the resulting typical performance parameters. In this work, two 3D filter membranes were constructed with MATLAB; one had a random distribution of unimodal nanofibers, and the other, a novel modification, formed a bimodal distribution; both of them had similar dimensions and solid volume fractions. A comparison of their performance in a dust-loading environment was made by using computational fluid dynamic-discrete element method (CFD-DEM) coupling technique in STAR-CCM+. It was found that the bimodal nanofiber membrane greatly improved the particle capture efficiency. Whereas this increased the pressure drop, the gain was not too significant. Thus, overall, the results of the figure of merit proved that adopting a bimodal formation improved the filter's quality.
Key words: 3D virtual filters, computational fluid dynamic (CFD), discrete element method (DEM), coupling simulation, dust loading, STAR-CCM+
CLC number: TQ 021.1 **Document code:** A

0 Introduction

Filtration is a multi-phase process in which the component phases interact in an intricate fashion. Particles are deposited on the porous filter structure whereas the fluid that carries them there goes on to permeate through the filter's pore network. During the initial stage of this process (also known as the clean filter phase), the quantity of the deposited particulate matter is not too significant to affect the filter's subsequent performance behavior. Due to the relative simplicity of this stage, most classical filtration theories were derived based on it[1-4]. However, filters deployed in their natural operating environments experience a sustained flow of contaminant-laced fluids which builds the chains of particulate matter on their surfaces; this process was first observed by Watson[5]. Taking a case of simple air filters, the sustained exposure to dust laden air will have it accumulating mostly on fibers at the upstream side where various adhesion/cohesion mechanisms keep them mutually bonded together or onto the fibers to form clusters[6-9]. For ordinary electrically neutral fine aerosols/dust particles of less than 50 μm in diameter, Bowling[10] noted that van der Waals forces remain their primary force of adhesion onto dry surfaces. The availability of particle structures on the filter surface and the severity of their packing density greatly affect the filter's subsequent performance raising both its inherent pressure drop and efficiency[11-13].

The use of idealized physical models in which the fluid flow process is solved by using algorithms helps to boost experiments especially in instances where certain variables are too complex to deal with experimentally[14]. In this work, two 3D filter membranes dissimilar in their internal microstructures but of the same dimensions and solid volume fraction (SVF) were fabricated by using MATLAB software. Then, a comparison of their performance in a dust-loading environment was made by using computational fluid dynamic-discrete element method (CFD-DEM) coupling technique.

Received: 2019-12-12 **Accepted:** 2020-01-05
Foundation item: the Chang Jiang Youth Scholars Program of China (No. 51773037), the National Natural Science Foundation of China (Nos. 51803023 and 61771123), the Shanghai Sailing Program (No. 18YF1400400), the China Postdoctoral Science Foundation (No. 2018M640317), and the Fundamental Research Funds for the Central Universities (No. 2232018A3-11)
∗**E-mail:** xhqin@dhu.edu.cn

1 Model Selection

1.1 Theory of Dendrite Formation

In a transient filtration regime, the particles will stick to each other. When this process goes on for a while, this kind of interaction results in the particle clusters that have independent physical properties, which affect the general properties and performance of the filter[15]. An example of these is the filter packing density. Accordingly, Thomas et al.[16] derived an expression that defines its heavy clogging regime by considering the mass of all the collected particles (M_p) on the filter's area (A_f):

$$\alpha_\mathrm{d} = \frac{M_\mathrm{p}}{A_\mathrm{f}\rho_\mathrm{p} z_\mathrm{d}}, \tag{1}$$

where, α_d is the packing density of the deposited particles; ρ_p is the particle density; z_d is the total density of the particle deposit.

Kanaoka and Hiragi[17] indicated that the particles do not accumulate homogeneously on the fibers. In which regard, they established a function for the dimensionless volume of collected particles (V'):

$$V' = \frac{4M_\mathrm{LF}}{\pi\rho_\mathrm{p} d_\mathrm{f}^2}, \tag{2}$$

where, M_LF is the mass of the collected particles per unit length of the fiber; d_f is the fiber diameter.

Also, Juda and Chrosciel[18] deduced a mathematical expression for the loaded filter's characteristic packing density (β) as a function of clean filter packing density (β_0), its volume (V_f) and V':

$$\beta = \beta_0 + \frac{V'}{V_\mathrm{f}} = \beta_0\left(1 + \frac{V'}{\beta_0 V_\mathrm{f}}\right). \tag{3}$$

On the other hand, Thomas et al.[19] did an experiment using particles of diameters: $d_\mathrm{p} = 2.6\,\mu\mathrm{m}$ and $d_\mathrm{p} = 0.15\,\mu\mathrm{m}$ as shown in Fig. 1(a). It was determined that at some point, these particles completely clogged the filter. Japuntich et al.[20] demonstrated that the agglomeration of particles as a result of particles loading on the filter surface, reduced the size of the available pores in the filter as shown in Fig. 1(b). This in turn increased the hydrodynamic drag experienced by the fluid as it went through the filter leading to a dynamic increase in pressure drop[21]. According to Bergman et al.[22], the dynamic loading of particles on the filter raised its pressure drop by a factor ΔP_p:

$$\Delta P = \Delta P_0 + \Delta P_\mathrm{p}, \tag{4}$$

where, ΔP is the overall pressure drop across a particle laden filter; ΔP_0 is the pressure drop across a clean filter.

In the same way, the increasing volume of particles piling up on the filter surface will offer a cumulative availability of surface upon which those particles that are still airborne can deposit. Accordingly, Kanaoka et al.[23] observed that the capture efficiency rising with the dynamic particle accumulation could be given by

$$\eta_\mathrm{m}/\eta_0 = 1 + \lambda_\mathrm{m}, \tag{5}$$

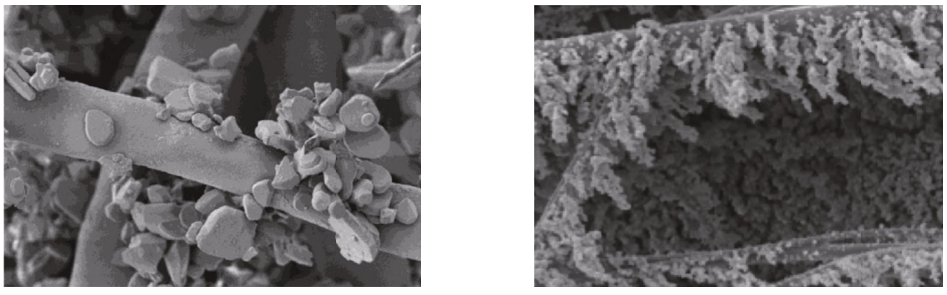

(a) Level of clogging attained with particles of diameter: d_p=2.6 μm and d_p=0.15 μm

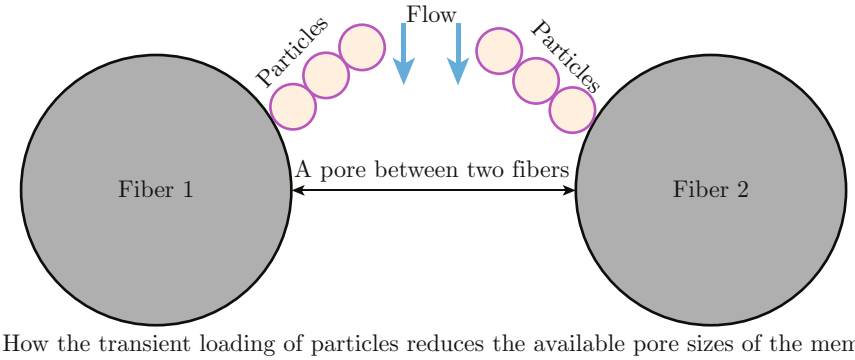

(b) How the transient loading of particles reduces the available pore sizes of the membrane

Fig. 1 Effect of transient particle loading on filter properties

where, η_{m} is the collection efficiency of a particle loaded fiber; η_0 is the collection efficiency of a clean fiber; λ_{m} is the loaded filter coefficient (collection efficiency raising factor).

1.2 CFD-DEM Coupled Process

Fluid and particle coupled systems consist of the continuous and the discrete phases flowing together, and the Eulerian-Lagrangian approach was used in modeling the transient accumulation of particulate matter. The continuous phase is characterized by pressure, velocity, and temperature while the discrete phase is defined by particulate concentration, velocity, temperature and position.

1.3 Computational Fluid Dynamics (CFD)

The above properties of the fluid streams were consolidated into mass, momentum and energy conservation, and the Navier-Stokes governing equations were used for evaluation. The flow was transient and laminar.

$$\nabla \cdot U_0 = 0, \tag{6}$$

$$\frac{\partial U_0}{\partial t} + u_0 \cdot \nabla U_0 = \nabla(p/\rho) + v\nabla \cdot \nabla U_0, \tag{7}$$

where, ∇ is the divergence operator; U_0 is the superficial velocity; t is the time; u_0 is the fluid's initial velocity; p is the fluid pressure; ρ is the fluid density; v is the overall fluid velocity.

1.4 Discrete Element Method (DEM)

The DEM used in the modeling of particle flows enables the tracking of individual particle motions, particle-particle interaction and fluid-particle interaction. Introduced by Cundall and Strack[24], it can conveniently handle the particle dynamics of all shapes and sizes. Normally, the active forces depend on the particle characteristics and the carrier fluid properties, which can be categorized into fluid-particle external forces ($\boldsymbol{f}_{\mathrm{ext}}$) and particle-particle contact forces ($\boldsymbol{f}_{\mathrm{con}}$), and harmonized into one function by using the Newton's second equation of motion.

$$m_{\mathrm{p}} \frac{\mathrm{d}^2 x}{\mathrm{d}t^2} = \left| \boldsymbol{f}_{\mathrm{con}} + \boldsymbol{f}_{\mathrm{ext}} \right|, \tag{8}$$

where, m_{p} is the mass of a single particle; $\mathrm{d}^2x/\mathrm{d}t^2$ is the second derivative of the particle path with respect to time.

DEM falls into two physics classifications, that is, soft sphere and hard sphere formulations. In the soft sphere method, bodies are considered deformable during collision, and deformation is taken into account via an overlap in force-displacement models. Forces acting between the two spheres are decomposed into normal and tangential components. In the hard sphere formulation, bodies are considered rigid with collisions taken instantaneously to register no deformations during the collision process. Soft sphere approach allows for multiple contacts and can be used to duly represent particle agglomerations experienced with particle loading. In this work, the major focus is on the agglomeration of particles on a filter surface, and soft sphere formulation is solved by a nonlinear viscoelastic model shown in Fig. 2 ($\boldsymbol{f}_{\mathrm{diss}}$ is the viscous force following a collision;

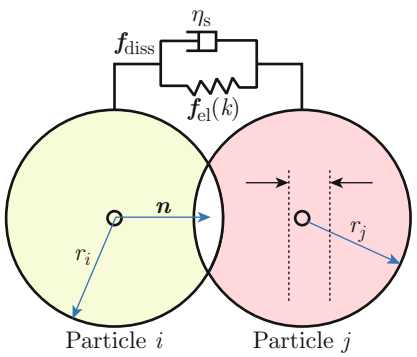

(a) Force-displacement model for contact between particles

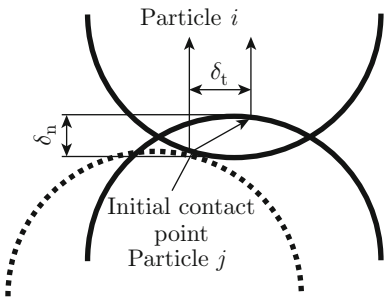

(b) Tangential particle contact process

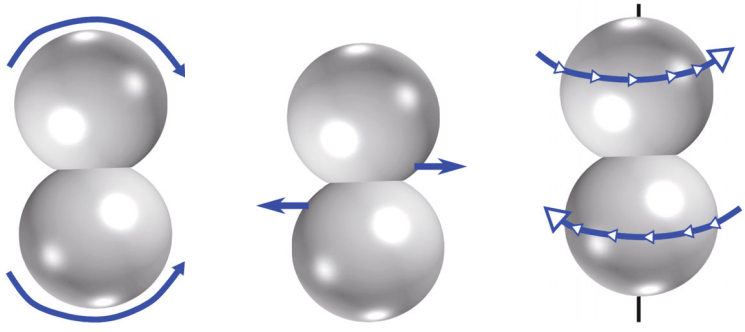

(c) Particle rolling (d) Particle sliding (e) Particle twisting

Fig. 2 Particle-particle interactions

$\boldsymbol{f}_{\mathrm{el}}(k)$ is the elastic collision force; k is the spring stiffness; η_{s} is the damping coefficient of the dashpot; $\boldsymbol{n}$ is the unit vector normal to the contact plane and pointing from particle i towards particle j; r_i is the radius of particle i; r_j is the radius of particle j; δ_{n} is the overlap of the particles in the normal direction; δ_{t} is the overlap of the particles in the tangential direction).

2 Simulation

2.1 Geometry Design and Computational Domain Set-up

Cylinders have finite dimensions such as length and diameter, and bear a close semblance to fibers. This makes it practical to use them in the precise representation and computation of various filter parameters for instance packing density, thickness and solid volume fraction. In this work, two different virtual filter membranes were built from a network of 3D cylinders generated via a MATLAB code. The first membrane was built from uniform fibers (1 μm in diameter) while in the second membrane, fibers that constituted 24% of its total SVF were reduced threefold to a diameter of 0.33 μm. Thus, a bimodal structure was created in which majority of the fibers were 1 μm in diameter.

Both of these structures were constructed by depositing cylinders randomly along the x- and y-axes which allowed the membrane thicknesses to grow along the z-axis thus occupying a 3D space of dimensions (50 μm × 50 μm × 8 μm). Despite the internal microstructure of the membranes differing on the basis of fiber diameter, their thicknesses and SVFs were maintained uniform for both. The SVF was determined by summing up the entire volume of cylinders (fibers) with the respective fiber and membrane volumes given by

$$V_{\mathrm{cyl}} = \pi r_{\mathrm{f}}^2 L, \tag{9}$$

$$V_{\mathrm{mod}} = V_{\mathrm{cyl}_1} + V_{\mathrm{cyl}_2} + \cdots + V_{\mathrm{cyl}_n}, \tag{10}$$

where, V_{cyl} is the cylinder volume; V_{mod} is the total volume of all the fibers in the membrane; V_{cyl_1}, V_{cyl_2}, V_{cyl_3} and V_{cyl_n} are the volumes of respective cylinders in the membrane; L is the length of each cylinder; n is the number of cylinders in the membrane; r_{f} is the cylinder radius.

Uniform fibers of diameter ($d_{\mathrm{f}} = 1$ μm) were used in the unimodal membrane shown in Fig. 3(a). Whereas, the bimodal membrane in Fig. 3(b) was a mixture of two fiber diameters ($d_{\mathrm{f1}} = 1$ μm and $d_{\mathrm{f2}} = 0.333$ μm). Both membranes had the same filter porosity ($\varepsilon = 0.86$). Before modeling them, appropriate computational domains were set up as enclosures within which the membranes were subjected to an uninterrupted flow of air. Similar domains were used for both models and these had dimensions of 52 μm × 52 μm × 30 μm as shown in Figs. 3(c) and 3(d). The air volume that extended beyond the upstream and downstream sides of the filter acted as the buffer zone to help establish the flow on both the upstream and downstream sides of the filter. Rebaï et al.[25] noted that this buffer zone ought to be big enough to avoid interactions between the inlet and the outlet.

The boundary conditions were a velocity inlet, a pressure outlet, symmetry sides and solid walls for the filter. Symmetry sides meant that the shear stress on these surfaces was zero.

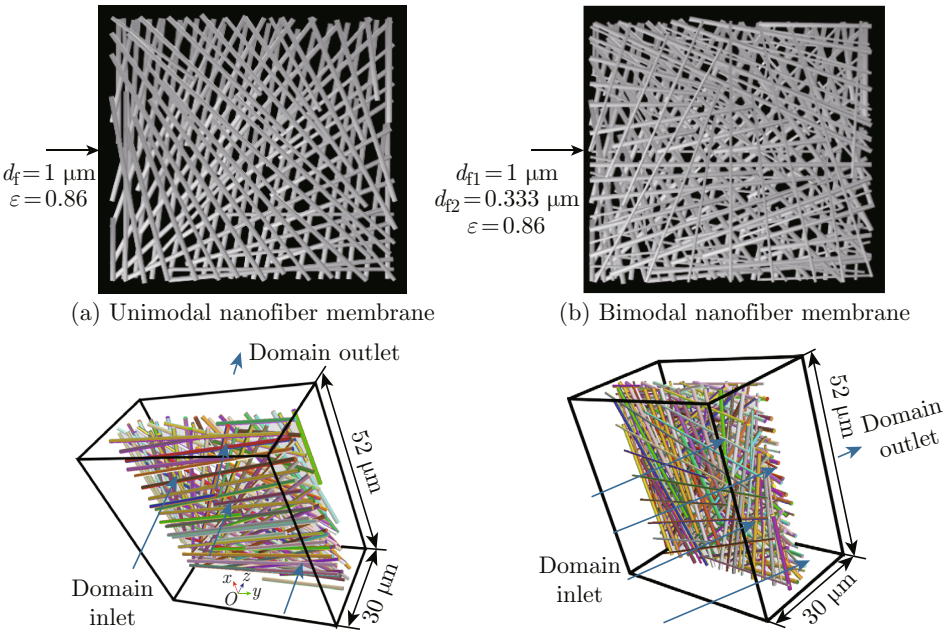

(a) Unimodal nanofiber membrane

(b) Bimodal nanofiber membrane

(c) Unimodal membrane within its computational domain

(d) Bimodal membrane within its computational domain

Fig. 3 Membrane models and computational domains of unimodal and bimodal nanofibers

2.2 Meshing Process and Mesh Independence Test

In simulation, meshing helps in geometry discretization, and its fineness influences both the precision of the final result and the calculation's computational burden. Accordingly, a polyhedral mesh was administered and this aptly controlled the distribution of grid points, giving them a larger and sparse grid in the bulk of the domain where there is an uninterrupted flow while the mesh was denser and more clustered near the walls (Fig. 4). In addition, a "mesh independence test" technique was applied to strike a balance between the accuracy and the computing resource requirement.

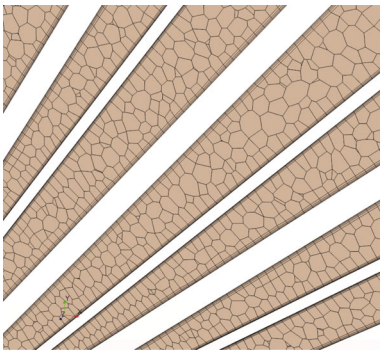

(a) Polyhedral mesh in 2D

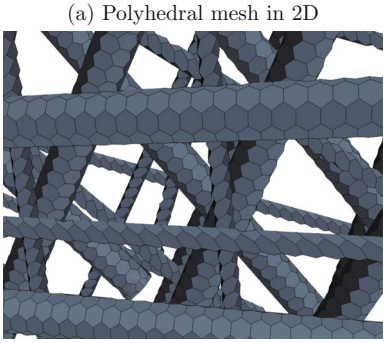

(b) Polyhedral mesh in 3D

Fig. 4 Details of mesh used on both membranes (representation was done by using bimodal membrane)

In this case, Ogorodnikov's derivation[26] for the pressure drop (ΔP) across a filter was used to study the mesh's element size significance on the pressure drop results.

$$\Delta P = \frac{4\mu U_0 \alpha H}{r_{\mathrm{f}}^2(-0.5\ln\alpha - 0.5)}, \tag{11}$$

where, μ is the fluid viscosity; H is the membrane thickness.

A unimodal nanofiber membrane structure is very close to what had been used in the equation's formulation, therefore, it was adopted for the validation process. Accordingly, the following values were chosen for the variables involved: $\mu = 1.855 \times 10^{-5}$, $\alpha = 01379$, $H = 8\,\mu\mathrm{m}$, $r_{\mathrm{f}} = 5\,\mu\mathrm{m}$, $U_0 = 0.1$, 0.2, 0.3, 0.4, 0.5 m/s. The corresponding values of pressure drop were given in Table 1.

Table 1 Face velocity and corresponding pressure drop from empirical formula

Velocity/(m·s^{-1})	ΔP/Pa
0.1	66.739
0.2	133.478
0.3	200.217
0.4	266.955
0.5	333.694

Pressure drop results corresponding with the number of cells achieved at each meshing regime were juxtaposed with the pressure drop calculated using the empirical function in Eq. (9). Mesh settings used to achieve the minimum error between these two were then selected as presented in Table 2.

Table 2 Results of mesh independence test to optimize simulation results

Test	Cells	Smallest cell/μm	Simulation ΔP/Pa	Empirical ΔP/Pa	Error/Pa
1	343 865	0.45	267.402	333.694	66.294
2	451 131	0.39	297.356	333.694	36.338
3	657 176	0.27	315.000	333.694	18.694
4	680 659	0.25	322.790	333.694	10.904
5	1 224 476	0.21	330.000	333.694	3.694

2.3 Simulation of Fluid-Particle Coupling and Particle Adhesion Processes

Coupling between these two involves an interactive exchange between their components during the flow. In a time-step dependent simulation, the results obtained in the current time-step become the starting point for the values at the next stage which helps to keep track of each individual particle's instantaneous flow path. The CFD provides the fluid flow profiles over the fluid cells allowing for the tracking of particle flow patterns until the deposition. Spherical elastic particles considered here were introduced into the flow by a part injector located near the domain's inlet, and the settings given in Table 3 were utilized in simulating the CFD-DEM coupling process.

The density of the virtual fibrous materials corresponded with that of polyacrylonitrile (PAN), which is one of the most commonly used polymers in the production of electrospun nanofibrous membranes for air filtration. On the other hand, the properties of the simulation process such as memory requirements speed greatly rely on the elastic modulus of the particles, where a very high elastic modulus often results in computationally expensive simulations. Accordingly, Hærvig et al.[27] found a way to ease on the time and resource requirements for DEM simulation by modifying the surface energy density (γ) of particles in the

Table 3 Settings utilized in CFD-DEM coupling simulation

CFD		DEM	
Model dimensions	3D	Particle type	DEM particles
Time	Implicit unsteady	Shape	Spherical
Material	Gas	Particle diameter/μm	0.5
Flow	Coupled	Material	Solid
Equation of state	Constant density	Equation of state	Constant density
Viscous regime	Laminar	Particle forces	Drag, shear lift and spin lift forces
Face velocity/$(\mathrm{m}\cdot\mathrm{s}^{-1})$	0.5	Model	2-way coupling

adhesive Johnson-Kendall-Roberts (JKR) contact and rolling model:

$$\gamma_{\mathrm{mod}} = \gamma \frac{E_{\mathrm{mod}}}{E}, \tag{12}$$

where, γ_{mod} is the modified surface energy density of the particles; E_{mod} is the modified elastic modulus; E is the normal elastic modulus.

With this change, the stick/rebound remained the same but the collision process took place over longer time periods allowing for higher time step sizes.

The fluid forces on the particles are dominated by the drag force (F_{d}) resulting from the relative velocities between the dispersed species and the fluid streamlines:

$$F_{\mathrm{d}} = \frac{v_{\mathrm{f}} - v_{\mathrm{p}}}{\tau_{\mathrm{p}}}. \tag{13}$$

Schiller Naumann drag correlation (C_{d}) was deemed the most applicable for this coupling regime:

$$F_{\mathrm{d}} = \frac{m_{\mathrm{p}}(v_{\mathrm{f}} - v_{\mathrm{p}})}{\tau_{\mathrm{p}} C_{\mathrm{d}}}, \tag{14}$$

$$C_{\mathrm{d}} = \begin{cases} \dfrac{24}{Re_{\mathrm{p}}}(1 + 0.15 Re_{\mathrm{p}}^{0.687}), & Re_{\mathrm{p}} \leqslant 10^3 \\ 0.44, & Re_{\mathrm{p}} > 10^3 \end{cases}, \tag{15}$$

where, τ_{p} is the time required for the particle to respond to change in fluid velocity; v_{f} is the fluid velocity; v_{p} is the particle velocity; Re_{p} represents the particle Reynolds's number.

The JKR particle adhesion model was adopted to account for the surface energy driven cohesive force responsible for holding the particles together and onto fibers after collision.

$$F_{\mathrm{cohesion}} = R_{\mathrm{min}} W_{\mathrm{coh}} \pi F, \tag{16}$$

where, R_{min} is the minimal radius of the surfaces in contact; W_{coh} is the work of cohesion, $\mathrm{J/m^2}$; F is a multiplication model-blending factor with a value of 1.5 for the JKR model.

Accordingly, the choice of the most appropriate work of cohesion value was guided by the Tabor factor:

$$\lambda_{\mathrm{T}} = \left(\frac{4R\gamma^2}{E^2 D_{\mathrm{min}}^3} \right)^{1/3}, \tag{17}$$

where, R is the effective particle radius; D_{min} is the minimum separation distance between particles.

Fibers were assigned a density of $1\,190\,\mathrm{kg/m^3}$, an elastic modulus of 3 GPa, a Poisson's ratio of 0.4, whereas particles were assigned a density of $1\,500\,\mathrm{kg/m^3}$, a Poisson's ratio of 0.3 and an elastic modulus of 2×10^7 Pa. These settings were very instrumental in particle-particle and particle-wall interactions. Overall, a work of cohesion of $0.000\,5\,\mathrm{J/m^2}$ was also adopted.

It should be noted that particle-particle and particle-wall interactions are characterized by the friction and the coefficient of restitution. A coefficient of restitution of 0.3 was used for both the impact of particles against particles and the particle-fiber impacts. Likewise, the friction played a role in the behavior of the particles during impact and adhesion processes. Thus, the values of 0.154 and 0.1 were adopted for the coefficients of static friction and rolling friction, respectively.

3 Results and Discussion

A number of factors including particle phase, particle size, and quantity of the deposited particles will influence the precise pattern and the morphology of the dendrites. In this work, the fluid flow velocity and the architecture of the filter's internal structure were concentrated on and utilized to compare the performance of the two membranes.

3.1 Particle Deposition Visualization

Filters comprise of several fiber layers, and each of them can potentially participate in capturing particles. However, in this case, the uppermost layer on the upstream side of the flow played a dominant role in trapping the oncoming particles, and as a result, dendrites were predominantly formed here (Fig. 5). Relatively fewer particles penetrated deeper within the membrane. Two phenomenal explanations can be given for this pattern: in some instances, the impact of particles with fibers in the top most layer could have been too weak to reduce their kinetic energy and bring them to a stop, whereby they continued ahead to deposit deeper within the membrane; another reason could have been that, particles followed the fluid flow streamlines through the pores to deposit on those fibers in the heart of the

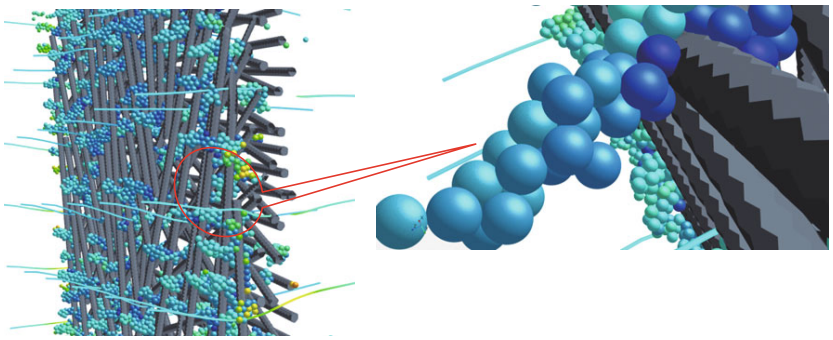

(a) Surface deposits on the unimodal membrane and the details of particle-particle and particle-fiber contacts

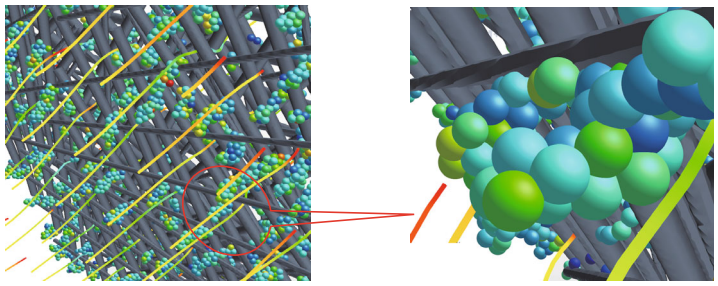

(b) Surface deposits on the bimodal membrane and the details of particle-particle and particle-fiber contacts

Fig. 5 Particle dendrites formation on the filter membrane and the fluid streamlines outlining the disruption caused by this formation on the fluid flow

membrane. These two points could also stand for particles that penetrated through the membrane. Particles were also observed to deposit mainly in the areas around the bigger membrane pores. This could be attributed to the conventional filter membrane's fabrication process, where fibers are randomly distributed to give an uneven pore distribution. Thus, the fluid flow through them tends to have more flux in bigger pores. Since fluid streamlines carry particles, deposition will be more concentrated in the areas of higher flow flux. All particle-particle interactions took place after deposition, and footprints of soft sphere contact are evident in the resulting particle contacts (Fig. 5).

In all, the initial simulation stages had fewer particle-particle contacts compared to the particle-wall contacts. This demonstrates a dominant role that the fibers play in the capture process at this point. However, a shift in this trend saw an exponential increase with time in the inter-particle contacts as manifested in Fig. 6. Another observation made was that, particle-particle and particle-wall contacts were more in number than the total particles injected into the domain. It is clear that during the agglomeration process, particles formed multiple contacts from various sides and a record of each of them was given, leading to a spike in the number of contacts.

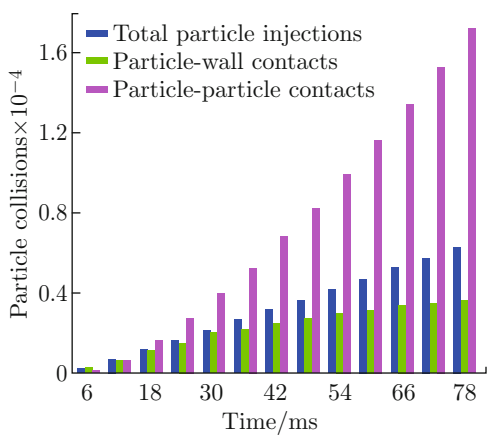

(a) Unimodal membrane

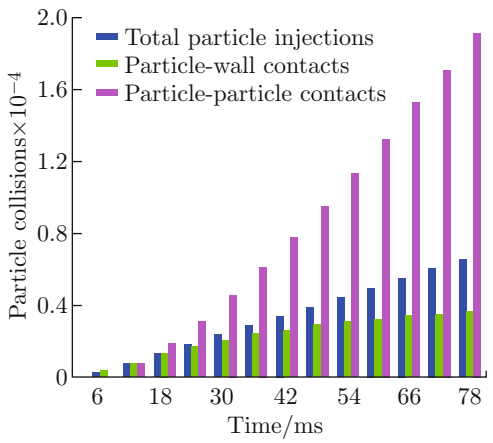

(b) Bimodal membrane

Fig. 6 Particle-particle and particle-wall interactions in relation to the total number of particles injected into the computational domain

3.2 Implication of Switching from Unimodal to Bimodal Structure on Pressure-Drop

Pressure drop is one of the two pillars of a filtration process, and this may determine if a filter is feasible. In this case, the simulation was conducted at a face velocity of 0.5 m/s, and a work of cohesion of 0.025 J/m^2 for particle-particle and particle-wall interactions. Prior to the particle loading regime, the unimodal nanofiber membrane and the bimodal membrane had a clean filter pressure drop of 283 Pa and 316.1 Pa, respectively. During the dynamic loading regime, pressure drop in both filter membranes rose steadily in response to the particles dynamically accumulating on the filter, and this was represented by polynomial linearly fitted plots in Fig. 7. Whereas the two display the similar trend, a steeper gradient is observed with the bimodal membrane which indicates a relatively higher particle loading rate. A higher particle loading rate is closely linked with a faster increase in the dynamic pressure drop.

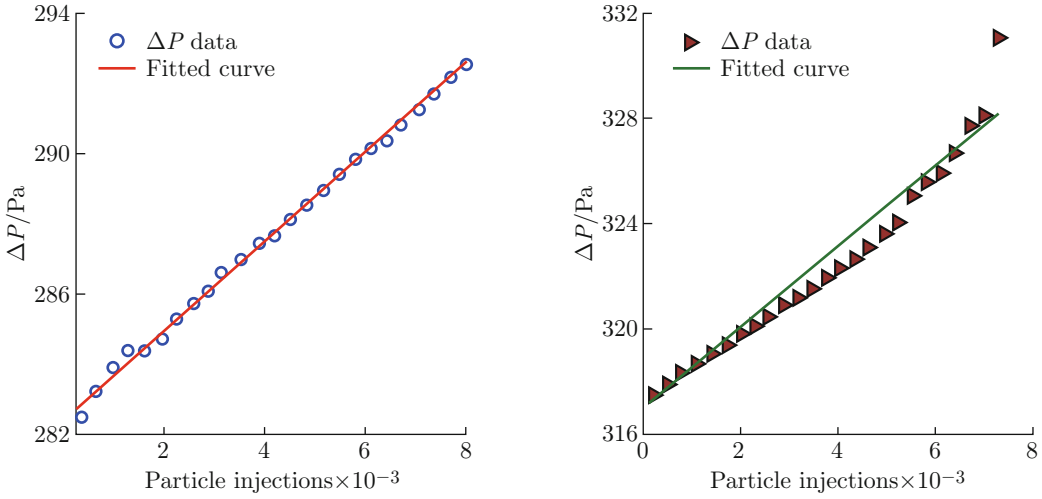

Fig. 7 Change in pressure drop of the unimodal and bimodal membranes with particle loading

To determine the gradient of the plots, a fitted curve linear model of $P_1X + P_2$ was used, with P_1 and P_2 points along the fitting line. For the unimodal membrane, the coefficients bound with 95% confidence were P_1 = 0.001 275(0.001 249, 0.001 302) and P_2 = 282.4(282.3, 282.5). For the bimodal model, the coefficients with 95% confidence bounds were P_1 = 0.001 634(0.001 48, 0.001 788) and P_2 = 316.1(315.5, 316.8).

3.3 Significance of Velocity on the Dynamic Loading Efficiency with Increasing Flow Velocity Magnitude

The flow properties of the carrier fluid strongly influence the particle flow and deposition. By considering a range of face velocity magnitudes (0.3, 0.5, 0.7, 1.0, 1.5, 2.0 m/s), the difference in performance of the two structures in a particle loading mode was investigated. In each of the cases, a full simulation run was performed over a number of time steps to achieve a fully loaded filter. Then the trend of particles' capture efficiency over this timeframe was examined. In addition, a laminar flow environment that upholds Darcy's law principles was adopted for all the studies. Conventionally, filtration efficiency of filters is determined by using multi-pass test (ISO 4548): a procedure corresponding to this method was applied to determine the dynamic particles' capture efficiency of the virtual filters used. This was achieved by putting provisions for counting particles both on the upstream and downstream sides of the filter. Then, the particle penetration was computed by

$$K = N/N_0, \tag{18}$$

From this, efficiency of the filter could be got from

$$\eta = 1 - K, \tag{19}$$

where, N is the number of particles going through the filter; N_0 is the number of particles injected into the filter; η is the membrane's particle capture efficiency.

Both membranes showed similar trends at the prevailing particle-particle and particle-wall cohesion/adhesion parameters used. Increasing the face velocity from 0.3 m/s to 0.7 m/s saw an increase in the capture efficiency of all the membranes (Fig. 8). However, as the fluid flow velocity increased to 1m/s and above, this trend declined. Increasing this velocity beyond a certain threshold led to the detachment of the loosely held particles. At higher velocities, when loose contacts between particles and the fibers are broken, it lowers the efficiency of the membrane. A change in microstructure from the unimodal to the bimodal

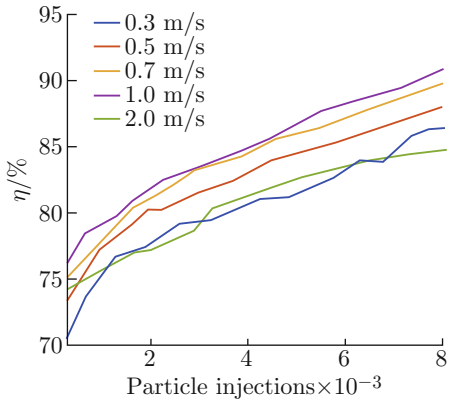

(a) Umimodal membrane

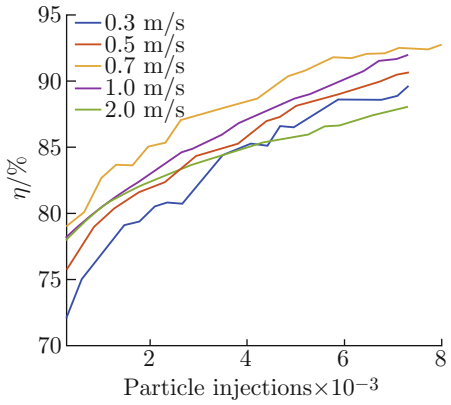

(b) Bimodal membrane

Fig. 8 Increase of filtration efficiency with fiber loading

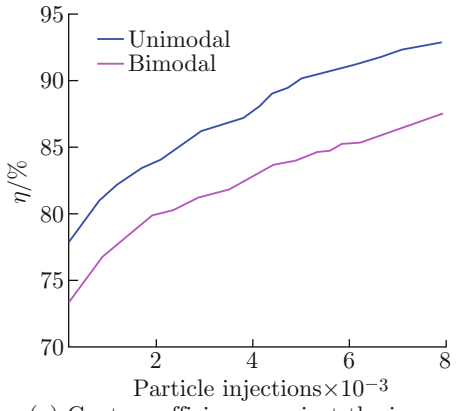

(a) Capture efficiency against the increasing number of particle injections

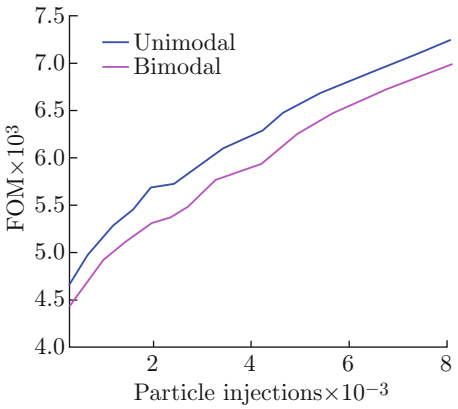

(b) FOM against the increasing number of particle injections

Fig. 9 Particle capture efficiency and FOM with filter cloggings

nanofiber membrane structure improved the dynamic efficiency of the fibrous media.

3.4 Significance of Change in Membrane Microstructure on Efficiency

Besides pressure drop, the other crucial element of filtration process is efficiency. This defines the percentage of total number of particles that a filter is able to intercept. The efficiency of the two media was compared and the better performing filter was determined by using the figure of merit (FOM) for each of the respective filter membranes during the dynamic particle accumulation phase (Fig. 9). The FOM is a benefit to cost ratio factor given by

$$\mathrm{FOM} = -\frac{\ln(1/K)}{\Delta P}. \tag{20}$$

Figure 9(a) shows that the bimodal membrane exhibited a much better filtration efficiency compared to the to the unimodal membrane. The improvement in the particle's capture efficiency can be attributed to the increased surface area that resulted from reducing the size of some fibers. However, this increased surface area increased the pressure drop of the bimodal membrane, which resulted in a relative drop in the FOM of the bimodal membrane. Despite this, overall, the bimodal membrane showed better filtration properties (Fig. 9(b)).

4 Conclusion

Filters operate in a transient environment characterized by time dependent accumulation of particles. However, most filter performance studies only deal with the clean filtration stage. In this work, a practical effort was made to investigate the performance of a filter during the dynamic loading process. Furthermore, regarding the performance of unimodal nanofiber membrane and a bimodal nanofiber membrane under dynamic particle loading conditions, it was observed that:

(1) CFD-DEM can be used to successfully model the dynamic particle growth on filters in a transient environment and give reliable data for the properties of these growths.

(2) Reducing the size of some of the fibers to create a bimodal arrangement tremendously improved the filter efficiency FOM of bimodal membranes.

It can be concluded that, using bimodal membranes improves the filter performance.

References

[1] SPIELMAN L, GOREN S L. Model for predicting pressure drop and filtration efficiency in fibrous media [J]. *Environmental Science & Technology*, 1968, **2**(4): 279-287.

[2] KIRSCH A A, FUCHS N A. Studies on fibrous aerosol filters. II. Pressure drops in systems of parallel cylinders [J]. *The Annals of Occupational Hygiene*, 1967, **10**(1): 23-30.

[3] HAPPEL J. Viscous flow relative to arrays of cylinders [J]. *AIChE Journal*, 1959, **5**(2): 174-177.

[4] KUWABARA S. The forces experienced by randomly distributed parallel circular cylinders or spheres in a viscous flow at small Reynolds numbers [J]. *Journal of the Physical Society of Japan*, 1959, **14**(4): 527-532.

[5] WATSON J H L. Filmless sample mounting for the electron microscope [J]. *Journal of Applied Physics*, 1946, **17**(2): 121-127.

[6] DALLAVALLE J M, ORR C, HINKLE B L. The aggregation of aerosols [J]. *British Journal of Applied Physics*, 1954, **5**(S3): S198-S206.

[7] ESMEN N A, ZIEGLER P, WHITFIELD R. The adhesion of particles upon impaction [J]. *Journal of Aerosol Science*, 1978, **9**(6): 547-556.

[8] STENHOUSE J I T, LLOYD P J, BUXTON R E. The retention of large particles ($> 2\,\mu$m) in fibrous filters [J]. *American Industrial Hygiene Association Journal*, 1976, **37**(7): 432-436.

[9] JORDAN D W. The adhesion of dust particles [J]. *British Journal of Applied Physics*, 1954, **5**(S3): S194-S197.

[10] BOWLING R A. A theoretical review of particle adhesion[M]//Particles on surfaces 1. Boston, USA: Springer, 1988: 129-142.

[11] THOMAS D, PENICOT P, CONTAL P, et al. Clogging of fibrous filters by solid aerosol particles experimental and modelling study [J]. *Chemical Engineering Science*, 2001, **56**(11): 3549-3561.

[12] LETOURNEAU P, VENDEL J, RENAUDIN V. Effects of the particle penetration inside the filter medium on the HEPA filter pressure drop [C]//*22nd DOE/NRC Nuclear Air Cleaning and Treatment Conference*. Denver, USA: IAEA, 1992.

[13] QIAN F, HUANG N, LU J, et al. CFD-DEM simulation of the filtration performance for fibrous media based on the mimic structure [J]. *Computers & Chemical Engineering*, 2014, **71**: 478-488.

[14] PAYATAKES A C. Model of transient aerosol particle deposition in fibrous media with dendritic pattern [J]. *AIChE Journal*, 1977, **23**(2): 192-202.

[15] TIEN C, WANG C S, BAROT D T. Chainlike formation of particle deposits in fluid-particle separation [J]. *Science*, 1977, **196**(4293): 983-985.

[16] THOMAS D, CHARVET A, BARDIN-MONNIER N, et al. Aerosol filtration [M]. Oxford, UK: Elsevier, 2016.

[17] KANAOKA C, HIRAGI S. Pressure drop of air filter with dust load [J]. *Journal of Aerosol Science*, 1990, **21**(1): 127-137.

[18] JUDA J, CHROSCIEL S. A theoretical model of pressure loss increase during the filtration process [J]. *Staub-Reinhaltung der Luft*, 1970, **30**(5): 12-15 (in German).

[19] THOMAS D, CONTAL P, RENAUDIN V, et al. Modelling pressure drop in HEPA filters during dynamic filtration [J]. *Journal of Aerosol Science*, 1999, **30**(2): 235-246.

[20] JAPUNTICH D A, STENHOUSE J I T, LIU B Y H. Effective pore diameter and monodisperse particle clogging of fibrous filters [J]. *Journal of Aerosol Science*, 1997, **28**(1): 147-158.

[21] PAYATAKES A C. Model of the dynamic behavior of a fibrous filter. Application to case of pure interception during period of unhindered growth [J]. *Powder Technology*, 1976, **14**(2): 267-278.

[22] BERGMAN W, TAYLOR R D, MILLER H H, et al. Enhanced filtration program at LLL: A progress report [C]//*17th DOE Nuclear Air Cleaning Conference*. Boston, USA: OSTI, 1978.

[23] KANAOKA C, EMI H, MYOJO T. Simulation of the growing process of a particle dendrite and evaluation of a single fiber collection efficiency with dust load [J]. *Journal of Aerosol Science*, 1980, **11**(4): 377-389.

[24] CUNDALL P A, STRACK O D L. A discrete numerical model for granular assemblies [J]. *Geotechnique*, 1979, **29**(1): 47-65.

[25] REBAÏM, DROLET F, VIDAL D, et al. A Lattice Boltzmann approach for predicting the capture efficiency of random fibrous media [J]. *Asia-Pacific Journal of Chemical Engineering*, 2011, **6**(1): 29-37.

[26] BUDYKA A K, OGORODNIKOV B I. Aerosol filtration (aerosol sampling by fibrous filters)[M]//Aerosols handbook. Boca Raton, USA: CRC Press, 2004: 541-556.

[27] HæRVIG J, KLEINHANS U, WIELAND C, et al. On the adhesive JKR contact and rolling models for reduced particle stiffness discrete element simulations [J]. *Powder Technology*, 2017, **319**: 472-482.